


## Exploring the effects of a one-dimensional periodic potential on a three-dimensional topological insulator

Albert Koop<sup>1,\*</sup>, Alexander Altmann<sup>1</sup>, Dmitriy A. Kozlov<sup>1,2</sup>, Nikolay N. Mikhailov<sup>2</sup>,  
Sergey A. Dvoretzskii<sup>2</sup> and Dieter Weiss<sup>1</sup>

<sup>1</sup>*Institute of Experimental and Applied Physics, University of Regensburg, D-93040 Regensburg, Germany*

<sup>2</sup>*A. V. Rzhanov Institute of Semiconductor Physics, Novosibirsk 630090, Russia*

 (Received 28 November 2023; revised 12 February 2024; accepted 16 February 2024; published 10 May 2024)

High mobility two-dimensional systems with superposed 1D lateral periodic potentials exhibit characteristic commensurability (Weiss) oscillations that reflect the interplay of the cyclotron radius at the Fermi level and the superlattice period. Here, we impose a one-dimensional periodic potential on strained HgTe, which is a strong 3D topological insulator. By tuning the Fermi level with top gates, the effects of the artificial potential can be studied in the bulk gap, where only Dirac surface states exist, in the conduction band, and in the valence band, where Dirac electrons and holes coexist. On the electron side, we observe clear commensurability oscillations whose period is governed by the carrier density of the top-surface Dirac electrons. Unexpectedly, weak commensurability oscillations are also observed in the valence band with a period that depends on both electron and hole density.

DOI: [10.1103/PhysRevResearch.6.023153](https://doi.org/10.1103/PhysRevResearch.6.023153)

### I. INTRODUCTION

Three-dimensional (3D) topological insulators (TIs) possess topologically protected, gapless metallic surface states that form a two-dimensional electron system (see [1] and references therein). The unusual properties of these interface states make TIs an interesting system, e.g., for spintronics and for the realization of topological superconductivity (see some examples in [2–6]). Although thousands of topological insulators have been identified to date [7–9], experimental studies have focused primarily on materials based on Bi, Hg, and Te. Strained HgTe, in particular, which is a strong topological insulator [10] is characterized by its high carrier mobility that allows the study of quantum effects like the quantum Hall effect in moderate magnetic fields [11–14]. TIs such as HgTe accommodate different types of carrier species, depending on the gate voltage applied. When the Fermi level is in the bulk gap [see Fig. 1(d)], only non-spin-degenerate topological surface states exist. These states are located on the top and bottom surfaces as well as on the side surfaces [14]. If the Fermi level is tuned to the conduction or valence band, bulk states also contribute to transport.

Here we study the magnetotransport of strained 3D-HgTe [15] subjected to a unidirectional periodic potential and a perpendicular magnetic field  $B$ . In topologically trivial, two-dimensional electron systems with high mobility, e.g., in semiconductor or oxide heterostructures and graphene, one

observes in such 1D lateral superlattices commensurability or Weiss oscillations (WOs) [17–23]. These oscillations reflect the interplay of the two characteristic lengths of the system, the cyclotron orbit radius  $R_C$ , and the period of the 1D periodic potential  $a$ . The resistance oscillates with  $1/B$  periodicity and displays minima whenever the condition

$$2R_c = 2 \frac{\hbar k_F}{eB} = \left( \lambda - \frac{1}{4} \right) a, \quad \lambda = 1, 2, 3, \dots \quad (1)$$

is met. Here,  $k_F$  is the Fermi wave vector,  $\hbar$  is the reduced Planck constant, and  $e$  is the elementary charge. The commensurability condition can be understood both semiclassically [24] and quantum mechanically [25]. When the commensurability condition Eq. (1) holds, electrons (holes) do not feel an electric field associated with the periodic potential on average along a cyclotron orbit so that the drift motion ( $\vec{E} \times \vec{B}$  drift) along the  $y$  direction vanishes [Fig. 1(c)]. In the quantum mechanical picture, the weak periodic potential lifts the Landau level degeneracy and leads to Landau bands  $E_n$  ( $n$  is the Landau band index) with a dispersion in the  $k_y$  direction. The commensurability condition Eq. (1) gives the energy and magnetic field values at which the dispersion vanishes and the bands become flat (flat band condition). At flat bands, the group velocity  $\propto \partial E_n / \partial k_y$ —the quantum mechanical pendant to the above drift velocity—vanishes [25]. A recently proposed alternative description attributes the  $1/B$  periodicity of WOs to the difference in the  $k$ -space areas  $S_0 - S_1$ . Here,  $S_0 = \pi k_F^2$  and  $S_1$  is the area of the first lens orbit in the  $k$  space created by Bragg reflection [26].

A particularly interesting aspect is that in HgTe the surface state band partially overlaps with the valence band [see Fig. 1(d)]. This means that at the corresponding positions of the Fermi level both electrons and holes move simultaneously under the influence of the periodic potential.

\*Corresponding authors: [albert.koop@ur.de](mailto:albert.koop@ur.de), [dieter.weiss@ur.de](mailto:dieter.weiss@ur.de)

Published by the American Physical Society under the terms of the [Creative Commons Attribution 4.0 International](https://creativecommons.org/licenses/by/4.0/) license. Further distribution of this work must maintain attribution to the author(s) and the published article's title, journal citation, and DOI.

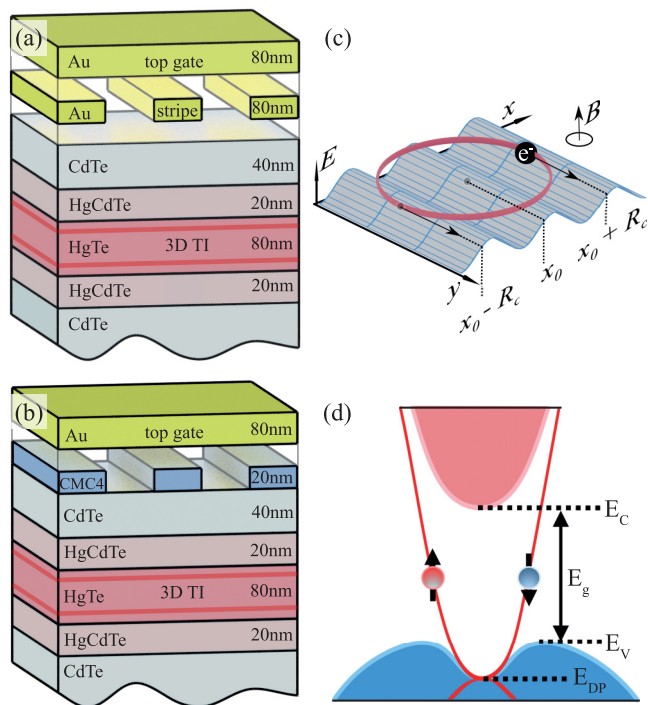


FIG. 1. (a) Cross section of the heterostructure with two gate layers called sample type A below. Numbers indicate the thickness of each layer. The fingers of the stripe gate of the lower gate are completely encapsulated in 30 nm/130 nm  $\text{SiO}_2/\text{Al}_2\text{O}_3$  insulator. The lattice constant  $a$  of the stripe gate is 500 nm (b) sample type B: Resist stripes made of the electron beam resist calixarene (p-chloromethyl-methoxy-calix[4]arene) create a 1D strain modulation with a largely constant amplitude. The carrier density can be varied by the planar top gate. The lattice constant is  $a = 300$  nm. (c) Cyclotron orbit in a one-dimensional periodic potential. The drift velocity in the  $y$  direction vanishes when the condition  $2R_c = (\lambda - \frac{1}{4})a$  holds. (d) Schematic band structure of strained HgTe with valence band (blue), conduction band (red), and non-spin-degenerate topological surface states. The Dirac point (DP) is buried in the valence band. Due to hybridization with the valence band, the Dirac electrons acquire a small mass causing the parabolic dispersion [11,15,16].  $E_C$  and  $E_V$  stand for the conduction band and valence band edge, respectively. The bulk gap  $E_g$  is of the order 15 meV.

## II. MATERIAL AND DEVICES

We use two different sample types named A [Fig. 1(a)] and B [Fig. 1(b)] integrated into a Hall bar geometry (width: 50  $\mu\text{m}$ , potential probe separation: 100  $\mu\text{m}$ ) to impose a 1D periodic potential on the 80 nm thick layer of HgTe. In the device type B sketched in Fig. 1(b), a unidirectional periodic potential is achieved by the strain pattern created by an array of 20 nm thick calixarene resist stripes [27], while the electron density can be varied by a single top gate. The device type A, which additionally allows tuning of the modulation strength, is sketched in Fig. 1(a) and consists of two gates: a stripe gate where all the stripes are connected to each other outside the transport channel and a planar top gate, which is separated from the stripe gate by 100 nm of oxide. By tuning the top gate voltage  $V_{tg}$  and the stripe gate voltage  $V_{sg}$ , both modulation strength and carrier density can be varied. The effect of both voltages on the longitudinal resistivity  $\rho_{xx}$  is shown

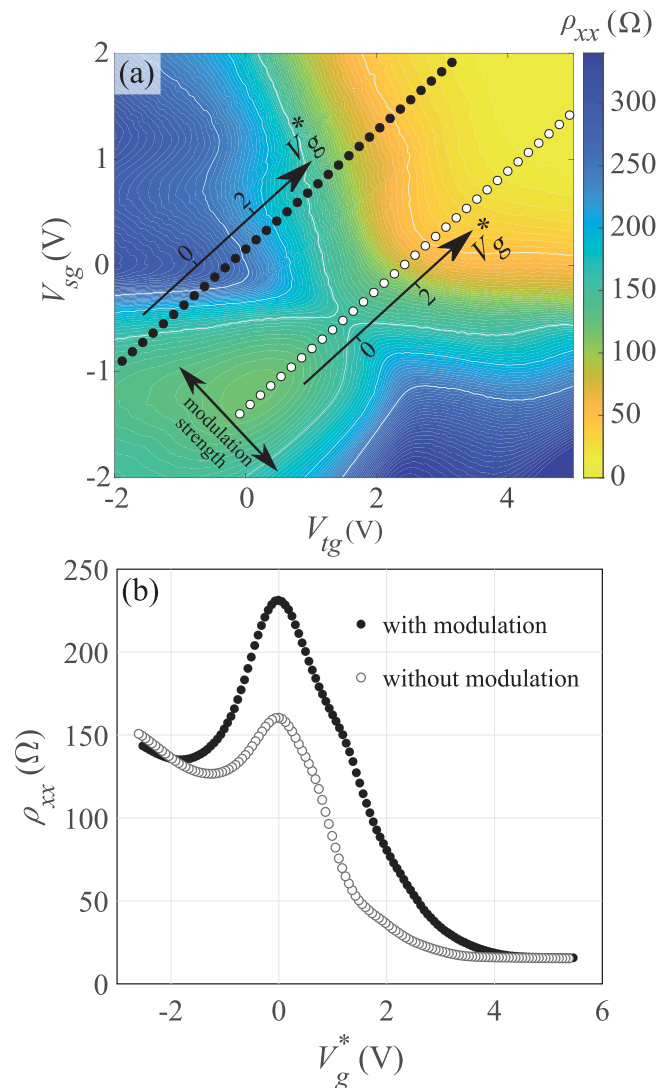


FIG. 2. (a) Gatemap for the sample type A with top and stripe gate [Fig. 1(a)]. The color scale shows the resistivity  $\rho_{xx}(\Omega)$  as a function of top gate voltage  $V_{tg}$  and stripe gate voltage  $V_{sg}$ . Along the line of white dots the modulation potential is minimal, while for voltages along the line of black dots, a weak, nearly constant modulation potential is present, causing commensurability oscillations. To represent the gate voltage dependencies  $V_{tg}$  and  $V_{sg}$  of  $\rho_{xx}$  along the black and white dotted lines, we introduce an effective 1D voltage scale  $V_g^* = (V_{tg} - V_{tg}^{CNP})\sqrt{1 + (dV_{sg}/dV_{tg})^2}$ , with its origin  $V_g^*(V_{tg}^{CNP})$  at the respective charge neutrality point. The corresponding voltage scales are shown on the color map. (b)  $\rho_{xx}$  vs  $V_g^*$  for the modulated (filled circles) and unmodulated (open circles) cases.

in Fig. 2(a). The arrows point in the direction of increasing electron density, while the modulation strength varies mainly along the direction perpendicular to the arrows. Along the line of open circles, the modulation strength is small, as indicated by the lowest measured resistance and suppression of WOs (not shown). In contrast, along the line of filled circles, the modulation potential has a higher, approximately constant amplitude, and the resistivity shows commensurability effects. The corresponding transport data are shown and discussed in the following. Figure 2(b) shows zero-field resistivity line

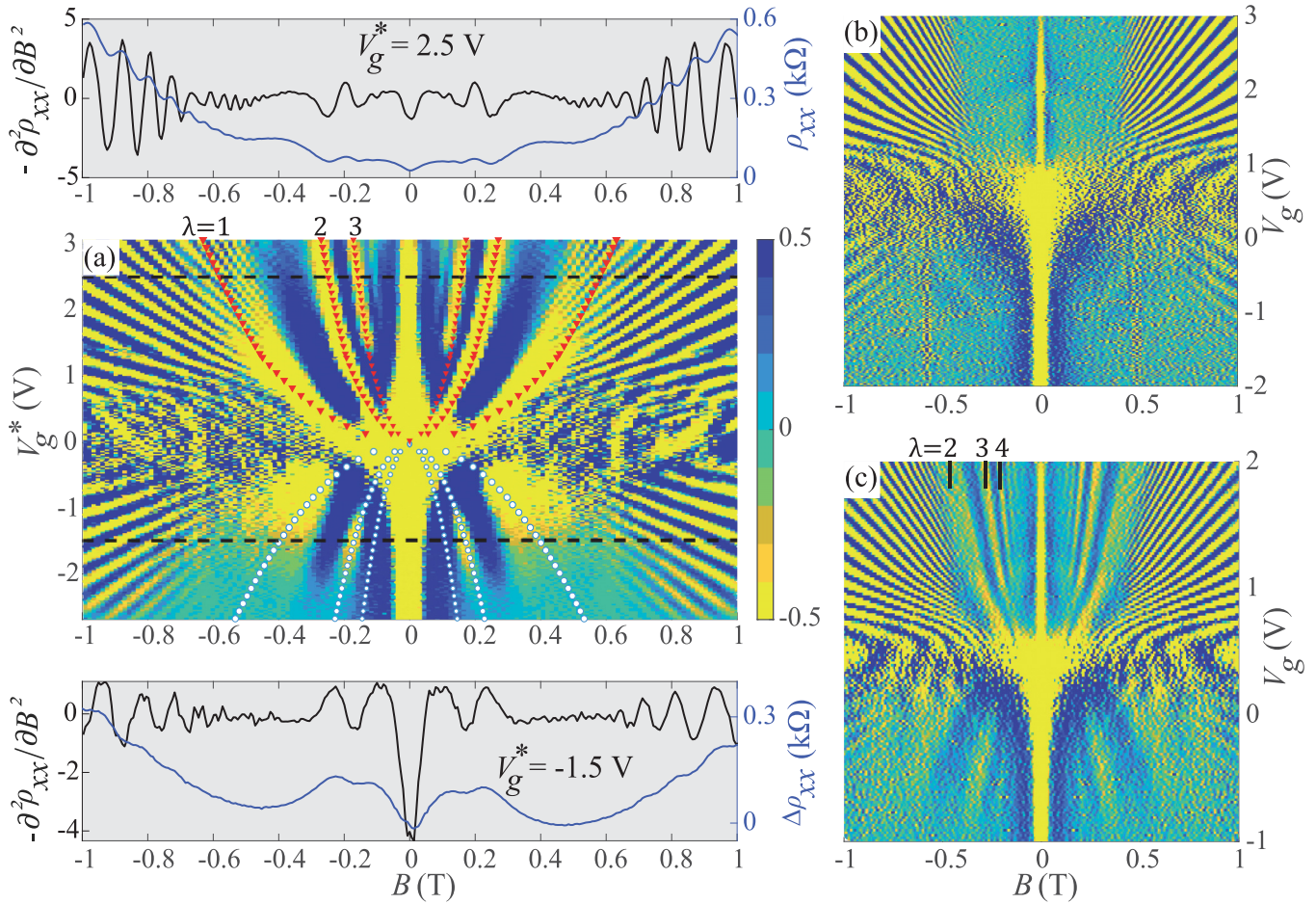


FIG. 3. The magnetoresistance  $\rho_{xx}(B)$ , its oscillatory part  $\Delta\rho_{xx}(B)$ , and its negative second derivative  $-\partial^2\rho_{xx}(B, V_g)/\partial B^2$ . (a) Data for device A at  $T = 295$  mK. The upper and lower panels display line scans of the magnetoresistance  $\rho_{xx}$  and the oscillatory component  $\Delta\rho_{xx}$  (in blue), respectively, as well as the negative second derivative (in black). The central panel shows the color map of the negative second derivative. The yellow color represents the minima and the blue color the maxima of  $\rho_{xx}$ . The parabolic features at small magnetic fields are due to commensurability and reflect the flat band condition, Eq. (1). Commensurability oscillations occur not only on the electron side but also, though weaker, in the valence band. Corresponding fits of the oscillation minima for the electron side (red triangles) and the valence band (white dots) are shown in the graph and discussed in the text. (b) The negative second derivative of the magnetoresistance of an unpatterned (only top gate) reference area of the same device at  $T = 1.4$  K. The color code is the same as in (a). While the SdH oscillations for holes and electrons are clearly visible, commensurability effects are absent. (c) The negative second derivative of the magnetoresistance for the sample type B with a fixed 1D modulation potential [Fig. 1(b)] was taken at  $T = 1.55$  K. The lattice period was  $a = 300$  nm, i.e., 40% smaller than in (a). Again, for this density-modulated system, the parabolic features at small fields are commensurability oscillations present on both the electron and valence band sides, but with 40% higher magnetic fields compared to the panel (a). For the highest positive gate voltage, WOs with  $\lambda$  up to six are resolved.

scans along full and open circles on the  $V_g^*$  effective voltage scale, defined in the figure caption. The increased resistivity for the modulated case indicates the presence of a 1D periodic potential. The gate voltage dependence of both  $\rho_{xx}$  traces is similar to that of planar-gate-only devices [12,14].

### III. TRANSPORT DATA

The color map Fig. 3(a) shows the negative second derivative of  $\rho_{xx}$  (which shows minima and maxima at the same position as  $\rho_{xx}$ , but enhanced) as a function of  $V_g^*$  and the magnetic field  $B$  at  $T = 295$  mK. Line plots of  $\rho_{xx}$  and  $-\partial^2\rho_{xx}/\partial B^2$  at  $V_g^* = 2.5$  V on the electron side and  $\Delta\rho_{xx}$  and  $-\partial^2\rho_{xx}/\partial B^2$  at  $V_g^* = -1.5$  V in the valence band are shown above and below the figure. The magnetoresistance

$\rho_{xx}$  in the top panel clearly shows Weiss oscillations at low  $B$ , which are enhanced in the negative second derivative of the data. The Shubnikov-de Haas (SdH) oscillations begin to appear at about 0.5 T. In the valence band (lower panel) the WOs are barely resolved in  $\rho_{xx}$  but visible in their oscillatory part  $\Delta\rho_{xx}$  when subtracting a linear background. In the two-dimensional  $-\partial^2\rho_{xx}/\partial B^2$  color map [central panel of Fig. 3(a)] in weak magnetic fields, the contributions from the WOs dominate. The resulting color pattern consists of upward- and downward-facing parabolas. The upward parabolas mirror Eq. (1). Since  $k_F \propto \sqrt{n}$  and the electron density  $n$  is proportional to  $V_g - V'$  ( $V'$  is an offset voltage that determines the carrier density at  $V_g = 0$ ), Eq. (1) reflects the relationship  $V_g - V' \propto B^2$ . Similar relations apply to holes for the downward parabolas. In the case of the double-gate

design A, the effective gate voltage  $V_g^*$  replaces  $V_g$ . Note that the electron (hole) density, represented by  $n$  ( $p$ ) in Eq. (1) refers only the carrier species that contribute to the formation of WOs. This partial density is also linearly dependent on the gate voltage. The parameters needed to describe the parabolic structures according to Eq. (1) are the respective partial filling rates  $\Delta n/\Delta V_g = \alpha_n$ . For holes,  $\Delta p/\Delta V_g = \alpha_p$  applies. Here,  $\alpha_i$  is defined as the filling rate of the respective carrier species. The filling rate depends on the position of the Fermi level and is different for  $E_F$  in the conduction band, the bulk gap, or the valence band [13,14]. This issue will be discussed in more detail below in the context of Fig. 4. At larger magnetic field values, linear Landau fans for electrons and holes dominate the color map. Figure 3(b), where the data have been taken from an unpatterned region with only one top gate, shows that the parabolic features, and thus the commensurability effects, are absent. Figure 3(c) illustrates that WOs can be observed not only in the stripe gate system A, but also in device type B where periodic density modulation has been achieved by using resist stripes that act as stressors and induce a periodic potential by the piezoelectric effect [27]. The parabolic fan in this device looks very similar to the one in Fig. 3(a).

To identify and fit the carriers involved in the formation of the parabolic fans in Fig. 3(a), one needs to know the partial densities and the corresponding filling rates of the different groups of carriers. Figure 4 shows the electron ( $n$ ) and hole densities ( $p$ ) for device A [Fig. 4(a)] and device B [Fig. 4(b)] at different gate voltages  $V_g^*$  and  $V_g$ , respectively. The system under study contains several types of electrons and bulk holes. We used different techniques, described in [12], to extract the carrier densities of the different charge carrier species, and the results are shown in Fig. 3: The linear Hall slope on the electron side gives the total electron density  $n_{\text{tot}}^{\text{Hall}}$ . The period of SdH oscillations at small magnetic fields on the  $n$  side gives the electron density  $n_{\text{top}}^{\text{SdH,low}}$  of the top surface. In the valence band, where surface electrons and bulk holes coexist, the electron density (sum of the top and bottom surface)  $n^{\text{Drude}}$  and hole density  $p^{\text{Drude}}$  can be extracted using the two-carrier Drude model. The hole density  $p^{\text{SdH}}(V_g^*)$  extracted from the SdH oscillations in the valence band is about the same as  $p^{\text{Drude}}(V_g^*)$ . The dependence of charge carrier densities on the gate voltage, shown in Fig. 4, are typical for 3D-HgTe [12,14].

The periodicity of the WOs on the electron side is perfectly described by using the carrier density  $n_{\text{top}}^{\text{SdH,low}}$  in Eq. (1). The corresponding calculated data are shown by the fan of red triangles in Fig. 3(a). Here, we have used the linearized electron density  $n_{\text{top}}^{\text{SdH,low}}$  [straight lines in Fig. 4(a)] and have taken into account that these surface states are not spin degenerate, that is, the relevant  $k_F$  vector is given by  $k_F = \sqrt{4\pi n_{\text{top}}^{\text{SdH,low}}}$ . We have also taken into account the change in the partial filling rate from  $\alpha_n = 0.9 \cdot 10^{15} \text{ m}^{-2}\text{V}^{-1}$  to  $\alpha_n = 0.6 \cdot 10^{15} \text{ m}^{-2}\text{V}^{-1}$  at  $V_g^* \approx 1.3 \text{ V}$ , when the Fermi level enters the conduction band [12,13]. The change in the filling rate is accompanied by faint but distinguishable kinks on the experimental fans and fits in Fig. 3(a). Using these experimental parameters perfectly describes the data without any fit parameter. The key result here is that the WOs on the electron side are determined solely

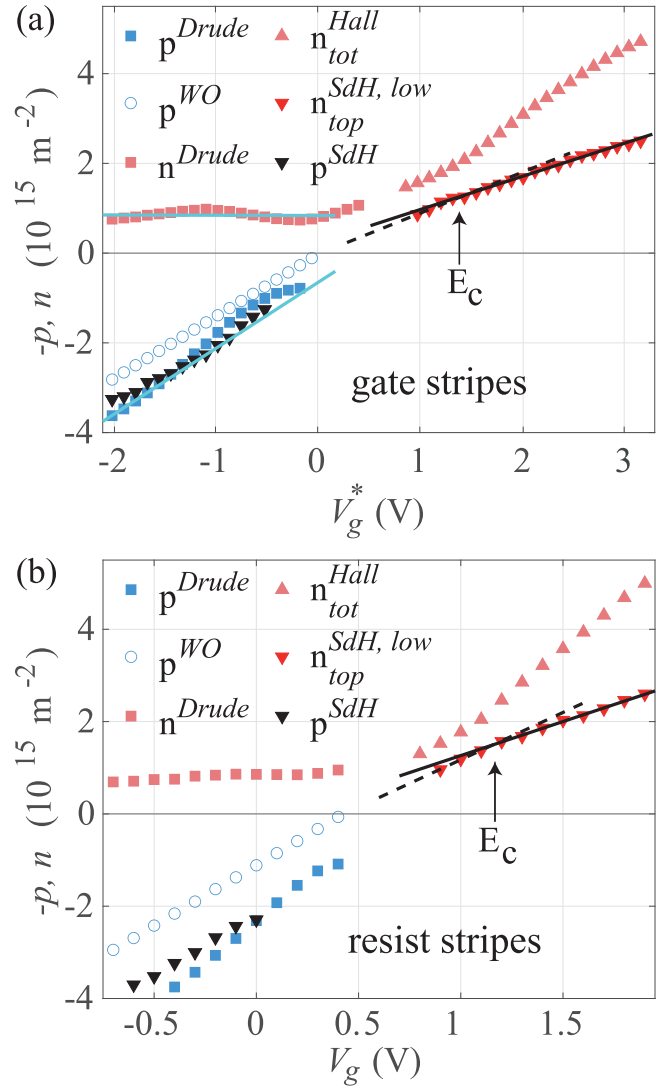


FIG. 4. (a) Partial and total electron  $n(V_g^*)$  and hole densities  $p(V_g^*)$  determined by four methods in sample A [Fig. 1(a)]. On the electron side, the Hall slope gives the total electron density (light red upward triangles) and the SdH oscillations at small magnetic fields yield the electron density of the top surface (dark red downward triangles). The black dashed and solid lines are the linear fit of the top surface electron density in the bulk energy gap and conduction band, respectively. Note the different slopes of these lines and hence the different partial filling rates. The lines cross at the bottom of the conduction band marked by the arrow  $E_c$ . On the hole side, the two-carrier Drude model gives the total electron and hole densities (light red and blue squares) and the SdH oscillations give the hole density (black downward triangles). In addition, we obtained the hole concentration by fitting the WOs (see text). The resulting hole concentration is shown by the open blue circles. (b) Same as (a) but for sample B with resist stripes [Fig. 1(b)].

by the carrier density of the top surface Dirac electrons. This is similar to the situation found in antidot superlattices [28].

#### IV. MODELLING OF WEISS OSCILLATIONS

The situation in the valence band is more subtle. This is also due to the fact that the commensurability features

are weak, though clearly visible as a parabolic fan chart in Fig. 3(a). Fitting the downward-facing parabolas with Eq. (1), assuming a constant filling rate as a fitting parameter and a twofold (spin) degeneracy, yields a hole density denoted as  $p^{WO}$ . The fit is shown as white dots in Fig. 3(a) and the resulting density is shown as open blue circles in Fig. 4. The density does not agree with the one extracted from the two-carrier Drude and the period of the SdH oscillations.

Here we have the situation that both electrons and holes can contribute to the commensurability oscillations. Since for both sample geometries, the periodic potential is also due to the piezoelectric potential, it is possible that the Dirac electrons at the bottom surface also feel the potential modulation potential because the thickness of the HgTe film is much smaller than the lattice constant  $a$ . On the electron side this does not appear to play a role because the potential amplitude is attenuated with increasing depth, and the WOs from the top surface dominate a potentially smaller effect from the back side. In the valence band, away from the flat band condition, the cyclotron orbits of electrons and holes are expected to drift in the same direction in a 1D periodic potential if they have the same diameter and center coordinate. It is currently unclear whether this joint drift motion of electrons and holes in the same direction increases or decreases the conductivity in the  $y$  direction. Therefore, we have performed simulations based on the two-component Drude picture. Within the semiclassical approach, the extra conductivity in the  $y$  direction due to a sinusoidal periodic potential in the  $x$  direction is given by

$$\Delta\sigma_{yy}^{e,h} \approx \frac{e^2}{2\pi\hbar} \frac{V_0^2}{\gamma\hbar\omega_c} \frac{4}{ak_F} \cos^2 \left[ 2\pi \frac{R_c}{a} - \frac{\pi}{4} \right], \quad (2)$$

with  $\gamma = \hbar/em^*\mu$  [18,29]. Here,  $m^*$  is the effective mass of the electrons or holes and  $V_0$  is the amplitude of the modulation potential. This extra conductivity exists for electrons and holes. In addition to the effective masses, the formula for electrons and holes differs in several other parameters, namely the cyclotron frequency  $\omega_c$ , the cyclotron radius  $R_c = \hbar k_F/(eB)$ , the mobility  $\mu$ , and the Fermi wave vector  $k_F$ .

We can now imagine two possible scenarios. In the first one, the extra conductivities for electrons and holes are added to the total conductivity. Here we have in mind that electrons and holes (which form a two-dimensional hole gas at negative gate voltages) provide two independent transport channels and the extra conductivities  $\Delta\sigma_{yy}^{e,h}$  in the  $y$  direction of electrons and holes due to the periodic potential must be added. Let us start with this approach. The extra band conductivity increases the total conductivity of electrons and holes,

$$\sigma_{yy} = \frac{en\mu_e}{1 + (\mu_e B)^2} + \frac{ep\mu_h}{1 + (\mu_h B)^2} \quad (3)$$

by the following contribution in the  $y$  direction

$$\Delta\sigma_{yy} = \Delta\sigma_{yy}^e + \Delta\sigma_{yy}^h. \quad (4)$$

Here, the indices “ $e$ ” and “ $h$ ” label electron and hole quantities, respectively. Apart from the conductivity  $\sigma_{yy}$ , the other Drude magnetotransport coefficients  $\sigma_{xx} = \sigma_{yy}$  and

$$\sigma_{xy} = -\sigma_{yx} = \frac{en\mu_e^2 B}{1 + (\mu_e B)^2} - \frac{ep\mu_h^2 B}{1 + (\mu_h B)^2} \quad (5)$$

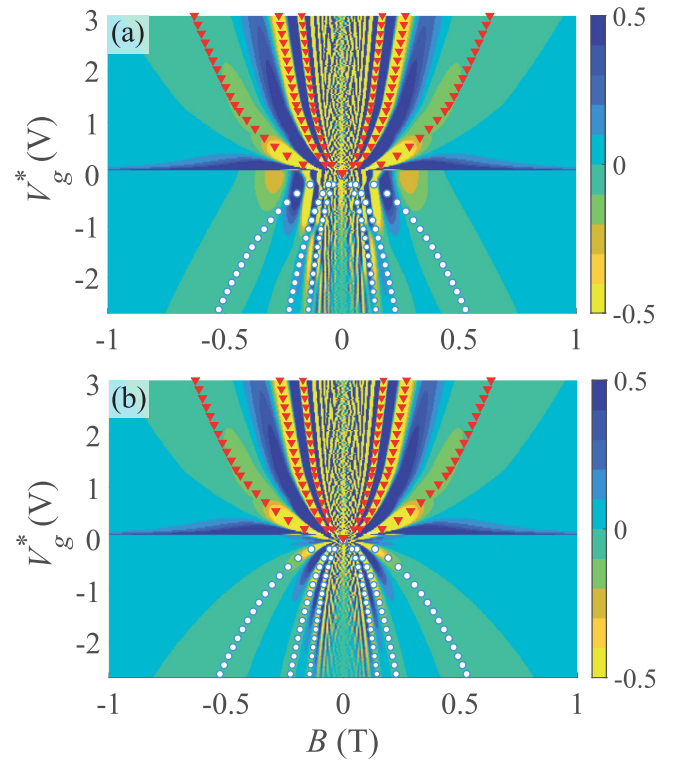


FIG. 5. The simulations of WOs: the calculated negative second derivative  $-\partial^2 \rho_{xx} / \partial B^2$  for the stripe gate sample A. The color code is the same as in Fig. 3, i.e., yellow represents the resistivity minima and blue represents the maxima. For the simulation, the gate-linearized carrier densities ( $n_{\text{top}}^{\text{SdH,low}}$ ,  $p^{\text{Drude}}$ ,  $n^{\text{Drude}}$ ) were taken from the experiment [straight lines in Fig. 4(a)]. For the description of the situation in the valence band, we assumed two scenarios. In (a) the extra conductivities in the  $y$  direction  $\Delta\sigma_{yy}^n$  for electrons ( $n^{\text{Drude}}$ ) and  $\Delta\sigma_{yy}^h$  for holes ( $p^{\text{Drude}}$ ) are added to the standard Drude conductivities in the valence band, i.e.,  $\sigma_{yy}^{\text{tot}} = \sigma_{yy}^e + \sigma_{yy}^h + \Delta\sigma_{yy}^e + \Delta\sigma_{yy}^h$ . The tensor inversion then yields  $\rho_{xx}$ . In (b) the charge carrier densities were subtracted,  $\Delta p = (p^{\text{Drude}} - n^{\text{Drude}})$ , and only the additional conductivity term ( $\Delta\sigma_{yy}^{\Delta p}$ ) was calculated using Eq. (2) and added to the valence band conductivities ( $\sigma_{yy}^{\text{tot}} = \sigma_{yy}^e + \sigma_{yy}^h + \Delta\sigma_{yy}^{\Delta p}$ ). To compare the calculations with the experiment, red triangles and white dots whose positions coincide with those in Fig. 3(a) and which denote the experimentally observed minima of the WOs are plotted on the color maps.

are not affected by the periodic potential in this approximation. The magnetotransport coefficient  $\rho_{xx}$  measured in the experiment is then obtained by tensor inversion and reads

$$\rho_{xx} = \frac{\sigma_{yy}^{\text{tot}}}{\sigma_{xx}\sigma_{yy}^{\text{tot}} - \sigma_{xy}\sigma_{yx}}. \quad (6)$$

Here,  $\sigma_{yy}^{\text{tot}} = \sigma_{yy} + \Delta\sigma_{yy}$ . To check the validity of the proposed approach, we calculated the magnetoresistance  $\rho_{xx}$  and its negative second derivative  $-\partial^2 \rho_{xx} / \partial B^2$  for the stripe gate sample. For the simulations, we used the linearized gate voltage densities [ $n_{\text{top}}^{\text{SdH,low}}$ ,  $p^{\text{Drude}}$ ,  $n^{\text{Drude}}$ , straight lines in Fig. 4(a)]. For the electron side we used the spin nondegenerate top surface electrons with mobility  $\mu_e = (34.8 + 30.6 \cdot V_g^*) \text{ m}^2/\text{V} \cdot \text{s}$ , estimated from the maximum number  $\lambda$  of observed WO, and a modulation amplitude of  $V_0^e = 2 \text{ meV}$ . In

the valence band we used the mobilities  $\mu_h = (15.4 + 3.25 \cdot V_g^*) \text{ m}^2/\text{V} \cdot \text{s}$  and  $\mu_e = (25.15 + 5.08 \cdot V_g^*) \text{ m}^2/\text{V} \cdot \text{s}$ . For the hole modulation potential we assumed a reduced amplitude of  $V_0^h = 0.2 \text{ meV}$  due to the screening by the surface states and the higher value of the hole effective mass. Note that the value of the amplitude does not affect the position of the minima and maxima, but rather the amplitude of the WOs. We used  $0.35m_0$  for holes [14,16] and  $0.028m_0$  for electrons [15] where  $m_0$  is the free electron mass. The result of the simulation is shown in Fig. 5(a). The color code is the same as in Fig. 3, i.e., yellow represents the resistivity minima, and blue represents the maxima. The experimental data, represented by the red triangles and white dots, correspond to the minima of the WOs and the flat band condition described by Eq. (1), as depicted in Fig. 3.

First, we consider the electron side (upper half) of the graph. The fan of red triangles shows remarkable agreement with the minima regions predicted by our model calculation. The white dot parabolas, which describe the minima of the commensurability oscillations on the hole side in Fig. 3(a) fit the calculated minima region less well. The maximum divergence is observed near the top of the valence band, i.e., in the range  $V_g^* = -0.5, \dots, 0 \text{ V}$ . This is partly because in the voltage range from about  $-0.5$  to  $0.5 \text{ V}$ , the underlying carrier densities are not directly accessible but are extrapolated. The lack of clear experimental WOs in this gate voltage range makes it impossible to draw firm conclusions. However, deeper in the valence band, there is also a difference in the positions of the calculated and experimental oscillation minima, indicating that the approach used is inaccurate.

Since the agreement between the experiment and model calculation on the hole side is not particularly satisfactory, we have investigated an alternative scenario. In the guiding center drift picture [24], both electrons and holes that have the same cyclotron orbit diameter and center coordinate drift in the same  $\pm y$  direction and could compensate for each other.

That is why it could be that we have to subtract the periodic potential induced electron and hole conductivities in Eq. (4). Calculations like the ones described above, but taking the difference of the hole and electron  $\Delta\sigma_{yy}$  conductivities, describe the experimental data even worse (not shown). The best agreement we obtained is when we assume that the surface electrons compensate for the holes and that the relevant  $k$  vector of the holes is given by  $k_F = \sqrt{2\pi(p-n)}$ . All the other parameters are the same as before in the calculations. A comparison of a model calculation using this expression in Eq. (2) to calculate the modulation-induced conductivity  $\Delta\sigma_{yy}$  in the  $y$  direction with the experimental result is shown in Fig. 5(b). While the agreement is remarkably good we cannot provide a microscopic picture of the compensation scenario. One could speculate, though, that the Coulomb interaction in the immediate vicinity of the surface states leads to bound electron-hole pairs [30] which do not participate in the guiding center drift.

In summary, we have studied magnetotransport in the 3D topological insulator HgTe with a superimposed weak 1D periodic potential. We found similar results regardless of the type of potential and its period. The commensurability (Weiss) oscillations, which reflect the commensurability between the cyclotron radius and the superlattice period, are dominated on the electron side by the Dirac electrons on the top surface. In the valence band, where bulk holes and Dirac electrons coexist, the period of the oscillations is best described by the difference in hole and electron densities, but an underlying model for this finding is lacking.

## ACKNOWLEDGMENTS

This work was supported by the European Research Council (ERC) under the European Union's Horizon 2020 research and innovation program (Grant Agreement No. 787515, "Promotion").

- 
- [1] M. Z. Hasan and J. E. Moore, Three-dimensional topological insulators, *Annu. Rev. Condens. Matter Phys.* **2**, 55 (2011).
- [2] Y. B. Fan, P. Upadhyaya, X. F. Kou, M. R. Lang, S. Takei, Z. X. Wang, J. S. Tang, L. He, L. T. Chang, M. Montazeri, G. Q. Yu, W. J. Jiang, T. X. Nie, R. N. Schwartz, Y. Tserkovnyak, and K. L. Wang, Magnetization switching through giant spin-orbit torque in a magnetically doped topological insulator heterostructure, *Nat. Mater.* **13**, 699 (2014).
- [3] E. Bocquillon, R. S. Deacon, J. Wiedenmann, P. Leubner, T. M. Klapwijk, C. Brüne, K. Ishibashi, H. Buhmann, and L. W. Molenkamp, Gapless andreev bound states in the quantum spin Hall insulator HgTe, *Nat. Nanotechnol.* **12**, 137 (2017).
- [4] H. Ren, F. Pientka, S. Hart, A. T. Pierce, M. Kosowsky, L. Lunczer, R. Schlereth, B. Scharf, E. M. Hankiewicz, L. W. Molenkamp, B. I. Halperin, and A. Yacoby, Topological superconductivity in a phase-controlled Josephson junction, *Nature (London)* **569**, 93 (2019).
- [5] O. Breunig and Y. Ando, Opportunities in topological insulator devices, *Nat. Rev. Phys.* **4**, 184 (2022).
- [6] R. Fischer, J. Picó-Cortés, W. Himmler, G. Platero, M. Grifoni, D. A. Kozlov, N. N. Mikhailov, S. A. Dvoretzky, C. Strunk, and D. Weiss,  $4\pi$ -periodic supercurrent tuned by an axial magnetic flux in topological insulator nanowires, *Phys. Rev. Res.* **4**, 013087 (2022).
- [7] T. Zhang, Y. Jiang, Z. Song, H. Huang, Y. He, Z. Fang, H. Weng, and C. Fang, Catalogue of topological electronic materials, *Nature (London)* **566**, 475 (2019).
- [8] M. G. Vergniory, L. Elcoro, C. Felser, N. Regnault, B. A. Bernevig, and Z. Wang, A complete catalogue of high-quality topological materials, *Nature (London)* **566**, 480 (2019).
- [9] M. G. Vergniory, B. J. Wieder, L. Elcoro, S. S. P. Parkin, C. Felser, B. A. Bernevig, and N. Regnault, All topological bands of all nonmagnetic stoichiometric materials, *Science* **376**, eabg9094 (2022).
- [10] L. Fu and C. L. Kane, Topological insulators with inversion symmetry, *Phys. Rev. B* **76**, 045302 (2007).
- [11] C. Brüne, C. X. Liu, E. G. Novik, E. M. Hankiewicz, H. Buhmann, Y. L. Chen, X. L. Qi, Z. X. Shen, S. C. Zhang, and L. W. Molenkamp, Quantum Hall effect from the topological surface states of strained bulk HgTe, *Phys. Rev. Lett.* **106**, 126803 (2011).

- [12] D. A. Kozlov, Z. D. Kvon, E. B. Olshanetsky, N. N. Mikhailov, S. A. Dvoretzky, and D. Weiss, Transport properties of a 3D topological insulator based on a strained high-mobility HgTe film, *Phys. Rev. Lett.* **112**, 196801 (2014).
- [13] D. A. Kozlov, D. Bauer, J. Ziegler, R. Fischer, M. L. Savchenko, Z. D. Kvon, N. N. Mikhailov, S. A. Dvoretzky, and D. Weiss, Probing quantum capacitance in a 3D topological insulator, *Phys. Rev. Lett.* **116**, 166802 (2016).
- [14] J. Ziegler, D. A. Kozlov, N. N. Mikhailov, S. Dvoretzky, and D. Weiss, Quantum Hall effect and Landau levels in the three-dimensional topological insulator HgTe, *Phys. Rev. Res.* **2**, 033303 (2020).
- [15] K. M. Dantscher, D. A. Kozlov, P. Olbrich, C. Zoth, P. Faltermeier, M. Lindner, G. V. Budkin, S. A. Tarasenko, V. V. Bel'kov, Z. D. Kvon, N. N. Mikhailov, S. A. Dvoretzky, D. Weiss, B. Jenichen, and S. D. Ganichev, Cyclotron-resonance-assisted photocurrents in surface states of a three-dimensional topological insulator based on a strained high-mobility HgTe film, *Phys. Rev. B* **92**, 165314 (2015).
- [16] J. Gospodarič, V. Dziom, A. Shuvaev, A. A. Dobretsova, N. N. Mikhailov, Z. D. Kvon, E. G. Novik, and A. Pimenov, Band structure of a HgTe-based three-dimensional topological insulator, *Phys. Rev. B* **102**, 115113 (2020).
- [17] D. Weiss, K. V. Klitzing, K. Ploog, and G. Weimann, Magnetoresistance oscillations in a two-dimensional electron gas induced by a submicrometer periodic potential, *Europhys. Lett.* **8**, 179 (1989).
- [18] R. W. Winkler, J. P. Kotthaus, and K. Ploog, Landau band conductivity in a two-dimensional electron system modulated by an artificial one-dimensional superlattice potential, *Phys. Rev. Lett.* **62**, 1177 (1989).
- [19] C. Nguyen, B. Brar, V. Jayaraman, A. Lorke, and H. Kroemer, Magnetotransport in lateral periodic potentials formed by surface-layer-induced modulation in InAs-AlSb quantum wells, *Appl. Phys. Lett.* **63**, 2251 (1993).
- [20] R. Yagi and Y. Iye, Oscillatory magnetoresistance in two-dimensional electron systems in a periodically modulated magnetic field, *J. Phys. Soc. Jpn.* **62**, 1279 (1993).
- [21] R. Cuscó, E. Skuras, S. Vallis, M. C. Holland, A. R. Long, S. P. Beaumont, I. A. Larkin, and J. H. Davies, Potential modulation under lateral surface superlattices, *Superlattices Microstruct.* **16**, 283 (1994).
- [22] K. Tanaka, J. Falson, Y. Kozuka, M. Uchida, D. Maryenko, J. T. Ye, Y. Iwasa, A. Tsukazaki, J. H. Smet, and M. Kawasaki, Ballistic transport in periodically modulated MgZnO/ZnO two-dimensional electron systems, *Appl. Phys. Lett.* **115**, 153101 (2019).
- [23] M. Drienovsky, J. Joachimsmeier, A. Sandner, M.-H. Liu, T. Taniguchi, K. Watanabe, K. Richter, D. Weiss, and J. Eroms, Commensurability oscillations in one-dimensional graphene superlattices, *Phys. Rev. Lett.* **121**, 026806 (2018).
- [24] C. W. J. Beenakker, Guiding-center-drift resonance in a periodically modulated two-dimensional electron gas, *Phys. Rev. Lett.* **62**, 2020 (1989).
- [25] R. R. Gerhardts, D. Weiss, and K. v. Klitzing, Novel magnetoresistance oscillations in a periodically modulated two-dimensional electron gas, *Phys. Rev. Lett.* **62**, 1173 (1989).
- [26] N. Paul, P. J. D. Crowley, T. Devakul, and L. Fu, Moiré Landau fans and magic zeros, *Phys. Rev. Lett.* **129**, 116804 (2022).
- [27] A. Endo and Y. Iye, Magnetoresistance of lateral hyperlattice: Independent control of spacing and phase of commensurability oscillation, *J. Phys. Soc. Jpn.* **69**, 3656 (2000).
- [28] H. Maier, J. Ziegler, R. Fischer, D. Kozlov, Z. D. Kvon, N. Mikhailov, S. A. Dvoretzky, and D. Weiss, Publisher correction: Ballistic geometric resistance resonances in a single surface of a topological insulator, *Nat. Commun.* **9**, 584 (2018).
- [29] C. Zhang and R. R. Gerhardts, Theory of magnetotransport in two-dimensional electron systems with unidirectional periodic modulation, *Phys. Rev. B* **41**, 12850 (1990).
- [30] N. F. Mott, The transition to the metallic state, *Philos. Mag.* **6**, 287 (1961).